


 Cite this: *RSC Adv.*, 2025, 15, 8346

# Insight into the key factors of $\beta$ -Mo<sub>2</sub>C catalyst for the reverse water gas shift reaction†

 Qingshan Rong,<sup>ab</sup> Wei Ding,<sup>b</sup> Guogang Liu,<sup>c</sup> Xiangyu Fu,<sup>b</sup> Yan Shi,<sup>d</sup> Zhiqiang Zhang <sup>\*a</sup> and Zhiwei Yao <sup>\*ab</sup>

In this study, we found that  $\beta$ -Mo<sub>2</sub>C prepared at different carbonization temperatures exhibited significantly different catalytic activities for the reverse water gas shift (RWGS) reaction. The  $\beta$ -Mo<sub>2</sub>C synthesized at 600 °C demonstrated notably higher activity compared to those prepared at 700 °C and 800 °C. This enhanced activity was likely attributed to its improved redox properties, which were primarily driven by a smaller crystallite size and the presence of Mo<sub>x</sub>OC<sub>y</sub> species. Therefore, we proposed that the crystallite size and Mo<sub>x</sub>OC<sub>y</sub> content were the key factors governing the RWGS activity of  $\beta$ -Mo<sub>2</sub>C. Clearly, both factors were strongly influenced by the carbonization temperature. Notably, the  $\beta$ -Mo<sub>2</sub>C prepared at 600 °C even outperformed Cu-doped  $\beta$ -Mo<sub>2</sub>C prepared at 700 °C under similar reaction conditions.

 Received 19th December 2024  
 Accepted 12th March 2025

DOI: 10.1039/d4ra08875a

[rsc.li/rsc-advances](https://rsc.li/rsc-advances)

## 1 Introduction

The heightened levels of carbon dioxide (CO<sub>2</sub>) in the atmosphere are widely acknowledged as a key contributor to climate change and ocean acidification.<sup>1</sup> Consequently, there has been considerable interest in capturing CO<sub>2</sub> and converting it into fuels and vital chemicals. The reverse water gas shift (RWGS) reaction is a promising pathway for CO<sub>2</sub> utilization, as the product CO can be directly utilized as a feedstock in the Fischer–Tropsch process, enabling further conversion into fuels and chemicals.<sup>2,3</sup>

Molybdenum carbide, in particular, has received much attention due to its capacity to facilitate both H<sub>2</sub> dissociation and C=O bond cleavage.<sup>4</sup> It was reported that Mo<sub>2</sub>C exhibited even higher activity and selectivity for the RWGS reaction compared to noble metal-based bimetallic catalysts such as PtCo/CeO<sub>2</sub> and PdNi/CeO<sub>2</sub>.<sup>5</sup> Since then, the molybdenum carbides have been widely studied as catalysts in the RWGS reaction and these studies mainly focus on the following aspects.<sup>6</sup> (i) The effect of crystal phase. To date, various phases of molybdenum carbide (*e.g.*,  $\alpha$ -MoC<sub>1-x</sub>,  $\beta$ -Mo<sub>2</sub>C and  $\alpha$ -Mo<sub>2</sub>C) have been investigated for the RWGS reaction.<sup>7–18</sup> It was found that  $\beta$ -Mo<sub>2</sub>C showed higher CO<sub>2</sub> conversion compared to  $\alpha$ -MoC<sub>1-x</sub> below 500 °C, but the latter exhibited higher CO

selectivity.<sup>8</sup> Very recently,  $\alpha$ -Mo<sub>2</sub>C had been discovered to be highly efficient and selective for the RWGS reaction.<sup>7,11</sup> This cubic molybdenum carbide can achieve equilibrium conversion and 100% CO selectivity at 600 °C for 500 h.<sup>11</sup> Additionally, Sun *et al.* had recently identified a unique Mo oxycarbide (Mo<sub>x</sub>OC<sub>y</sub>) structure that formed *in situ* on the surface of Mo oxide during the RWGS reaction. This structure was demonstrated to be more active than Mo carbide in the process.<sup>15</sup> (ii) The effect of support. Various common supports, such as  $\gamma$ -Al<sub>2</sub>O<sub>3</sub>, SiO<sub>2</sub>, SBA-15, CN and CNTs, had been utilized for supporting Mo<sub>2</sub>C in the RWGS process.<sup>19–24</sup> It was suggested that these supports generally offered surfaces for Mo<sub>2</sub>C dispersion and contributed to its stabilization against high-temperature sintering during the reaction.<sup>20</sup> (iii) The effect of metal promoter. Promotion of molybdenum carbides with other metals (*e.g.* Co, Cu, Na, K and Cs) also significantly modified the activity, selectivity and stability in the RWGS reaction.<sup>5,19,25–31</sup> Zhang *et al.* demonstrated that the strong interaction between Cu and  $\beta$ -Mo<sub>2</sub>C played a pivotal role in enhancing Cu dispersion and preventing agglomeration.<sup>25</sup> This phenomenon contributed significantly to the remarkable activity and stability. Additionally, Cs-doped Mo<sub>2</sub>C catalysts can exhibit higher CO selectivity than non-doped one.<sup>27</sup> The authors suggested that the electropositive nature of Cs facilitated electron transfer from Cs to Mo, resulting in a surface enriched with electrons, thereby favoring CO production.

Among these research strategies, modifying  $\beta$ -Mo<sub>2</sub>C with a metal, particularly Cu, has been regarded as one of the most effective methods to enhance catalyst's performance. However, the key factors influencing the RWGS activity of  $\beta$ -Mo<sub>2</sub>C remained unclear. In this study, for the first time, we found that  $\beta$ -Mo<sub>2</sub>C prepared at different carbonization temperatures exhibited significantly different RWGS activities. Interestingly,

<sup>a</sup>School of Chemical Engineering, University of Science and Technology Liaoning, Anshan, 114051, P.R. China. E-mail: zhangzhiqiang@ustl.edu.cn; mezhwei@163.com

<sup>b</sup>School of Petrochemical Engineering, Liaoning Petrochemical University, Fushun, 113001, P.R. China

<sup>c</sup>PetroChina Fushun Petrochemical Company, Fushun, 113008, P.R. China

<sup>d</sup>School of Chemistry and Materials Engineering, Huizhou University, Huizhou, 516007, P.R. China

† Electronic supplementary information (ESI) available. See DOI: <https://doi.org/10.1039/d4ra08875a>



the carbonization temperature had a greater effect on RWGS activity than the Cu promoter. Herein, the key factors governing the RWGS activity of  $\beta$ -Mo<sub>2</sub>C were clarified.

## 2 Experimental

### 2.1 Sample preparation

$\beta$ -Mo<sub>2</sub>C was synthesized using the traditional CH<sub>4</sub>/H<sub>2</sub>-temperature-programmed reduction method. Ammonium paratungstate ((NH<sub>4</sub>)<sub>6</sub>Mo<sub>7</sub>O<sub>24</sub>·4H<sub>2</sub>O; purchased from Aladdin Biochemical Technology Co. Ltd) was heated to 500 °C at 10 °C min<sup>-1</sup> and held at this temperature for 4 h to prepare precursor MoO<sub>3</sub> in a muffle furnace. Initially, 1.0 g of MoO<sub>3</sub> precursor was loaded into a micro-reactor. A flow of 20%CH<sub>4</sub>/H<sub>2</sub> (300 ml min<sup>-1</sup>) was then introduced into the system. The temperature was raised from room temperature (RT) to 300 °C over 30 min, followed by a further increase to a specified temperature at a rate of 1 °C min<sup>-1</sup>. Subsequently, the temperature was maintained at this level for 2 h before rapid cooling to RT under a 20%CH<sub>4</sub>/H<sub>2</sub> flow. Finally, the material underwent passivation in 1%O<sub>2</sub>/Ar for 2 h prior to exposure to air. Samples obtained from heating at 600, 700, and 800 °C were labeled as  $\beta$ -Mo<sub>2</sub>C-600,  $\beta$ -Mo<sub>2</sub>C-700, and  $\beta$ -Mo<sub>2</sub>C-800, respectively. The precursor for the Cu/ $\beta$ -Mo<sub>2</sub>C catalyst was synthesized *via* a coprecipitation method. A mixed aqueous solution containing (NH<sub>4</sub>)<sub>6</sub>Mo<sub>7</sub>O<sub>24</sub>·4H<sub>2</sub>O and Cu(NO<sub>3</sub>)<sub>2</sub>·6H<sub>2</sub>O, with a Cu content of 1 wt% relative to MoO<sub>3</sub>, was stirred at RT for 4 h. Subsequently, it was dried using a water bath at 80 °C, followed by overnight drying at 110 °C, and then calcination at 500 °C for 4 h to obtain the precursor. The carbonization and passivation processes followed a similar approach to the temperature-programmed reaction method described above. The samples synthesized at 600 and 700 °C were designated as 1 wt%Cu/ $\beta$ -Mo<sub>2</sub>C-600 and 1 wt%Cu/ $\beta$ -Mo<sub>2</sub>C-700, respectively.

### 2.2 Sample characterizations

X-ray diffraction (XRD) analysis was conducted employing an X-ray diffractometer (X'Pert Pro MPD) featuring a Cu K $\alpha$  source. The average crystallite size of  $\beta$ -Mo<sub>2</sub>C was calculated using the Scherrer equation  $d = 0.9\lambda/(B \cdot \cos \theta)$ , where  $\lambda$  was the X-ray wavelength (0.15406 nm),  $B$  was the peak width at half peak height in radians, and  $\theta$  was the angle between the incident and diffracted beams in degrees. Scanning electron microscopy (SEM) and transmission electron microscopy (TEM) images were obtained using Hitachi S-4800 instrument and Philips Tecnal 10 microscope, respectively. The BET surface area of the samples was determined using a Nova 4200e instrument from Quantachrome. X-ray photoelectron spectroscopy (XPS) was conducted utilizing a Kratos Axis ultra (DLD) instrument equipped with an Al K $\alpha$  X-ray source. The binding energies ( $\pm 0.2$  eV) were calibrated to the C 1s peak at 284.8 eV, attributed to adventitious carbon. H<sub>2</sub>-TPR experiments were conducted in a quartz tube micro-reactor, with effluent gases monitored using a thermal conductivity detector. Prior to each H<sub>2</sub>-TPR run, the samples (0.1 g) were subjected to heating from RT to 300 °C in a He atmosphere and maintained at this temperature for

30 min. Subsequently, the sample was cooled back to 100 °C before undergoing further heating from 100 to 900 °C at a rate of 10 °C min<sup>-1</sup> in a gas mixture of 5%H<sub>2</sub>/Ar (30 ml min<sup>-1</sup>). CO<sub>2</sub>-TPO was conducted using a flow of 6%CO<sub>2</sub>/Ar (50 ml min<sup>-1</sup>). Prior to the reaction, the  $\beta$ -Mo<sub>2</sub>C-600,  $\beta$ -Mo<sub>2</sub>C-700, and  $\beta$ -Mo<sub>2</sub>C-800 samples were preheated in H<sub>2</sub> at temperatures of 600, 700 and 800 °C, respectively, for a duration of 30 min. Subsequently, they were cooled to RT under Ar before being heated under the reactant gas from RT to 900 °C at a rate of 4 °C min<sup>-1</sup>. The gas-phase product evolution during the reaction was monitored using gas chromatography (GC). CO-TPD experiments were carried out in a quartz tube micro-reactor. Prior to the CO-TPD process, 0.1 g of catalyst underwent the same pretreatment procedures as those employed for the CO<sub>2</sub>-TPO.

After being cooled to RT in He flow, a stream of 10%CO/He was introduced into the system for 20 min. After CO adsorption, the gas flow was switched to He (30 ml min<sup>-1</sup>) to remove physically adsorbed CO on catalyst surface 30 min. Finally, the sample was heated from RT to 900 °C at a rate of 10 °C min<sup>-1</sup> in He (30 ml min<sup>-1</sup>), and then was held at 900 °C for 30 min. The effluent gases were monitored by means of a GC thermal conductivity detector.

### 2.3 Catalyst performance tests

The catalytic performance of the catalyst for the RWGS reaction was evaluated using a micro-reactor with an inner diameter of 8 mm. Prior to the reaction, the  $\beta$ -Mo<sub>2</sub>C-600,  $\beta$ -Mo<sub>2</sub>C-700, and  $\beta$ -Mo<sub>2</sub>C-800 samples were preheated in H<sub>2</sub> at temperatures of 600, 700 and 800 °C, respectively, for a duration of 30 min. Subsequently, a gas mixture consisting of H<sub>2</sub> and CO<sub>2</sub> in a ratio of 2 : 1 was introduced into the catalyst bed. The gas-phase products were continuously monitored using online GC. The conversion of CO<sub>2</sub>, the selectivities of CO and CH<sub>4</sub> as well as carbon balance were determined as follows:

$$\text{CO}_2 \text{ conversion (\%)} = ([\text{CO}_2]_{\text{in}} - [\text{CO}_2]_{\text{out}})/([\text{CO}_2]_{\text{in}}) \times 100$$

$$\text{CO selectivity (\%)} = ([\text{CO}]_{\text{out}})/([\text{CO}]_{\text{out}} + [\text{CH}_4]_{\text{out}}) \times 100$$

$$\text{CH}_4 \text{ selectivity (\%)} = ([\text{CH}_4]_{\text{out}})/([\text{CO}]_{\text{out}} + [\text{CH}_4]_{\text{out}}) \times 100$$

$$\text{Carbon balance (\%)} = ([\text{CO}_2]_{\text{out}} + [\text{CO}]_{\text{out}} + [\text{CH}_4]_{\text{out}})/([\text{CO}_2]_{\text{in}}) \times 100$$

## 3 Results and discussion

The XRD patterns of the  $\beta$ -Mo<sub>2</sub>C catalysts obtained at different carbonization temperatures of 600, 700 and 800 °C are shown in Fig. 1. The diffraction peaks at 34.5, 38.0, 39.6, 52.3, 61.9, 69.8, 75.0 and 76.0° were corresponded to the (100), (002), (101), (102), (110), (103), (112) and (201) reflections of  $\beta$ -Mo<sub>2</sub>C (JCPDS 65-8766). As the carbonization temperature increased from 600 to 800 °C, the diffraction peaks became sharper and more intense, indicating the enhanced crystallinity of  $\beta$ -Mo<sub>2</sub>C. Therefore, it was reasonable to estimate the crystallite size of  $\beta$ -



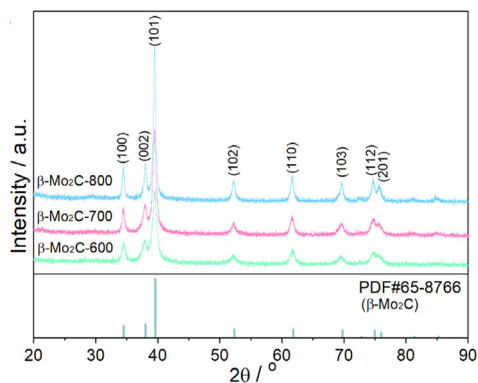


Fig. 1 XRD patterns of the  $\beta$ -Mo<sub>2</sub>C catalysts obtained at different carbonization temperatures of 600, 700 and 800 °C.

Table 1 BET surface area and crystallite size of the  $\beta$ -Mo<sub>2</sub>C catalysts obtained at different carbonization temperatures of 600, 700 and 800 °C

Sample	BET surface area (m <sup>2</sup> g <sup>-1</sup> )	Crystallite size (nm)
$\beta$ -Mo <sub>2</sub> C-600	34.0	20
$\beta$ -Mo <sub>2</sub> C-700	30.3	34
$\beta$ -Mo <sub>2</sub> C-800	17.9	45

Mo<sub>2</sub>C-600,  $\beta$ -Mo<sub>2</sub>C-700, and  $\beta$ -Mo<sub>2</sub>C-800 samples using the Scherrer method as 20, 34 and 45 nm, respectively (see Table 1). The increase in crystallite size corresponded to a decrease in surface area. It was well known that the complete synthesis process involved reduction-carbonization of MoO<sub>3</sub> precursor by 20%CH<sub>4</sub>/H<sub>2</sub> mixture *via* the pathway of MoO<sub>3</sub> → MoO<sub>2</sub> → Mo<sub>x</sub>OC<sub>y</sub> →  $\beta$ -Mo<sub>2</sub>C.<sup>32</sup> This process was strongly influenced by temperature and contact time, with the formation of the Mo<sub>x</sub>OC<sub>y</sub> phase typically occurring between 500 and 650 °C. Due to the broad XRD peaks ( $2\theta = 37$  and  $44^\circ$ ) associated with Mo<sub>x</sub>OC<sub>y</sub>,<sup>33</sup> they can easily be masked by the  $\beta$ -Mo<sub>2</sub>C peaks, making it difficult to exclude the presence of this phase in the  $\beta$ -Mo<sub>2</sub>C-600 sample.

The crystallite size of  $\beta$ -Mo<sub>2</sub>C was calculated by Scherrer equation according to (101) plane.

The morphologies of these  $\beta$ -Mo<sub>2</sub>C catalysts were observed using SEM and TEM (refer to Fig. 2). All three samples exhibited similar irregular particle aggregates. Detailed analysis of primary particle sizes using TEM was not easy due to significant agglomeration. Therefore, it must be taken into account the average size measured from XRD. The insets in Fig. 2a displayed EDX element mapping images, confirming the presence of Mo, C, and O elements in the  $\beta$ -Mo<sub>2</sub>C samples, and those in Fig. 2b clearly showed the  $\beta$ -Mo<sub>2</sub>C (002) crystal lattices, proving the existence of  $\beta$ -Mo<sub>2</sub>C phase in these samples. It was worth noting that the MoOC (111) crystal lattice, as reported by Sun *et al.*,<sup>15</sup> was also observed in multiple regions (more than three) of the  $\beta$ -Mo<sub>2</sub>C-600 sample (Fig. 2 and S1†), providing strong evidence for the coexistence of  $\beta$ -Mo<sub>2</sub>C and Mo<sub>x</sub>OC<sub>y</sub> phases. Moreover, the H<sub>2</sub>-TPR result (Fig. 3) demonstrated an obvious hydrogen

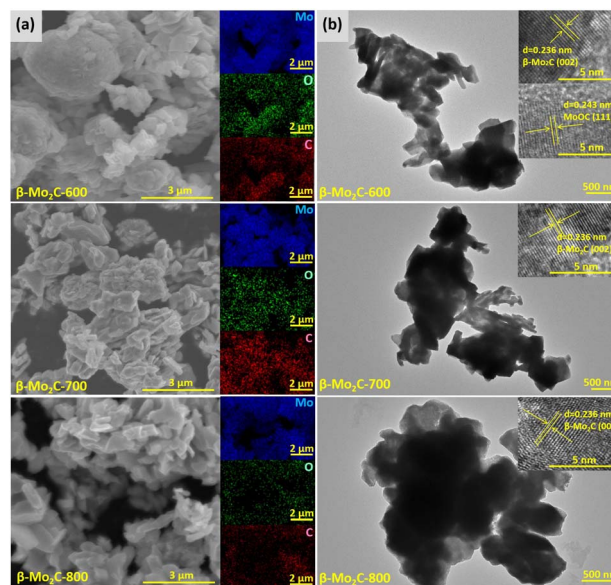


Fig. 2 (a) SEM images and (b) TEM images of  $\beta$ -Mo<sub>2</sub>C-600,  $\beta$ -Mo<sub>2</sub>C-700, and  $\beta$ -Mo<sub>2</sub>C-800 catalysts. The insets in the SEM images show the Mo, O and C element mapping images and those in the TEM images show the  $\beta$ -Mo<sub>2</sub>C (002) and MoOC (111) crystal lattices.

consumption peak when non-passivated  $\beta$ -Mo<sub>2</sub>C-600 was subjected to further treatment in a 5% H<sub>2</sub>/Ar atmosphere, thereby confirming the presence of Mo<sub>x</sub>OC<sub>y</sub> species. In contrast, the non-passivated  $\beta$ -Mo<sub>2</sub>C-700 and  $\beta$ -Mo<sub>2</sub>C-800 samples showed no H<sub>2</sub>-TPR signal, further confirming that they contained only the  $\beta$ -Mo<sub>2</sub>C phase.

Subsequently, further information regarding these  $\beta$ -Mo<sub>2</sub>C surfaces was obtained by XPS. Fig. 4 shows the XPS spectra of Mo 3d for the  $\beta$ -Mo<sub>2</sub>C-600,  $\beta$ -Mo<sub>2</sub>C-700, and  $\beta$ -Mo<sub>2</sub>C-800 catalysts. Based on the curve fitting of Mo 3d levels, Table 2 summarizes the Mo 3d<sub>5/2</sub> binding energy, distribution of Mo

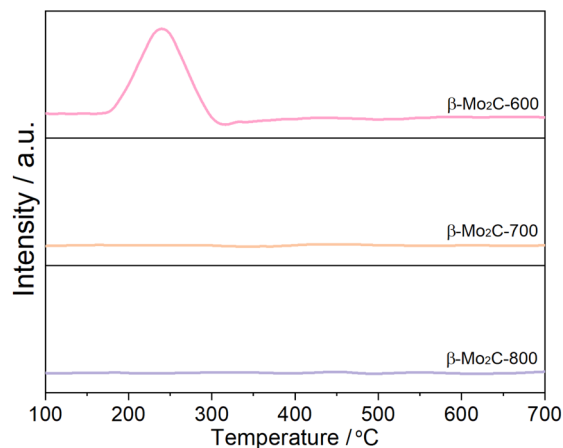


Fig. 3 H<sub>2</sub>-TPR profiles of non-passivated  $\beta$ -Mo<sub>2</sub>C-600,  $\beta$ -Mo<sub>2</sub>C-700, and  $\beta$ -Mo<sub>2</sub>C-800 catalysts. The non-passivated samples were directly subjected to H<sub>2</sub>-TPR experiment, where they were heated from 100 to 700 °C at a rate of 5 °C min<sup>-1</sup> in a gas mixture of 5%H<sub>2</sub>/Ar (60 ml min<sup>-1</sup>).



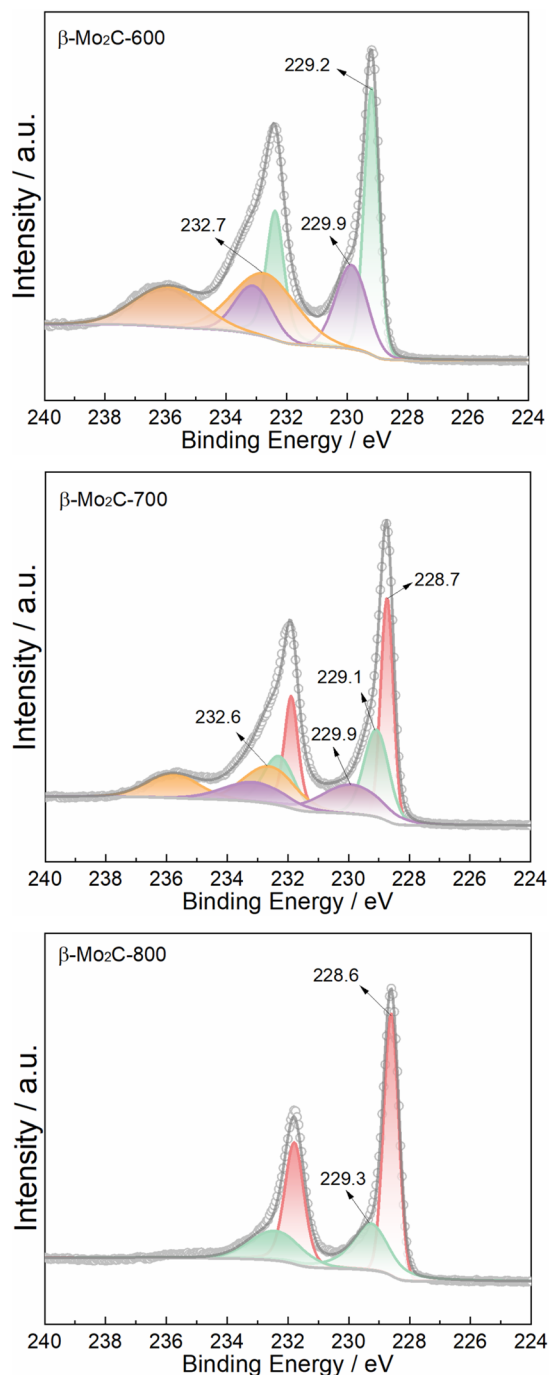


Fig. 4 XPS spectra of Mo 3d region of  $\beta$ -Mo<sub>2</sub>C-600,  $\beta$ -Mo<sub>2</sub>C-700, and  $\beta$ -Mo<sub>2</sub>C-800 catalysts.

species and Mo<sup>2+</sup> content. Because the as-prepared metal carbides were usually passivated before exposure to air, the surface regions of all the samples should be dominated by oxidized species and the underlying (oxy)carbide species. As shown in Fig. 4 and Table 2, four Mo 3d<sub>5/2</sub> binding energy peaks were observed on the  $\beta$ -Mo<sub>2</sub>C-700 surface at 228.7, 229.1, 229.9 and 232.6 eV. These peaks were assigned to Mo<sup>2+</sup> (carbide),<sup>34,35</sup> Mo<sup>δ+</sup> (oxycarbide),<sup>36,37</sup> Mo<sup>4+</sup> (oxide)<sup>38</sup> and Mo<sup>6+</sup> (oxide),<sup>39</sup> respectively. However, unlike  $\beta$ -Mo<sub>2</sub>C-700, the surfaces of  $\beta$ -Mo<sub>2</sub>C-800 and  $\beta$ -Mo<sub>2</sub>C-600 showed only two (Mo<sup>2+</sup> carbide and Mo<sup>δ+</sup> oxycarbide) and three Mo species (Mo<sup>δ+</sup> oxycarbide, Mo<sup>4+</sup> oxide and Mo<sup>6+</sup> oxide), respectively. The Mo<sup>2+</sup> contents of the  $\beta$ -Mo<sub>2</sub>C-600,  $\beta$ -Mo<sub>2</sub>C-700, and  $\beta$ -Mo<sub>2</sub>C-800 samples estimated by quantitative XPS analysis (Table 2) were 0, 32.0 and 63.2%, respectively. This indicated that the oxophilicity ranked in the order of  $\beta$ -Mo<sub>2</sub>C-600 >  $\beta$ -Mo<sub>2</sub>C-700 >  $\beta$ -Mo<sub>2</sub>C-800.

The RWGS performance variation of the  $\beta$ -Mo<sub>2</sub>C-600,  $\beta$ -Mo<sub>2</sub>C-700, and  $\beta$ -Mo<sub>2</sub>C-800 catalysts with temperature is shown in Fig. 5a, b and S2.† A clear correlation was observed between the carbonization synthesis temperature and the RWGS activity, with  $\beta$ -Mo<sub>2</sub>C-600 exhibiting the highest activity, followed by  $\beta$ -Mo<sub>2</sub>C-700 and  $\beta$ -Mo<sub>2</sub>C-800 in the entire temperature range. Arrhenius curve is presented in Fig. 5c. The E<sub>a</sub> values followed the order of  $\beta$ -Mo<sub>2</sub>C-800 >  $\beta$ -Mo<sub>2</sub>C-700 >  $\beta$ -Mo<sub>2</sub>C-600, which was just the opposite of their ranks in RWGS activity. To compare the influence of carbonization synthesis temperature and Cu doping on the RWGS activity of  $\beta$ -Mo<sub>2</sub>C, a Cu-doped  $\beta$ -Mo<sub>2</sub>C catalyst was synthesized at 700 °C (XRD pattern shown in Fig. S3†). The crystallite size of  $\beta$ -Mo<sub>2</sub>C in this Cu doped catalyst was estimated to be 31 nm. Noticeably, the  $\beta$ -Mo<sub>2</sub>C-600 even displayed slightly higher RWGS activity compared to Cu-doped  $\beta$ -Mo<sub>2</sub>C-700 under similar reaction conditions. In terms of selectivity, although CO selectivities increased with carbonization synthesis temperature, they can remain above 95% throughout the entire temperature range. The main side product was CH<sub>4</sub>, resulting from the methanation of CO<sub>2</sub>. And the carbon balances ranged from 0.98 to 1.00 (see Fig. S2†). The errors in CO<sub>2</sub> conversion, CO/CH<sub>4</sub> selectivity as well as carbon balance were all within ±2%, which was consistent with previously reported results and deemed acceptable.<sup>40</sup> Finally, the catalytic stability of the  $\beta$ -Mo<sub>2</sub>C-600,  $\beta$ -Mo<sub>2</sub>C-700, and  $\beta$ -Mo<sub>2</sub>C-800 catalysts at 600 °C was depicted in Fig. S4.† It was evident that all three catalysts exhibited excellent stability throughout the 10 h test period. Given the superior performance of the  $\beta$ -Mo<sub>2</sub>C-600 catalyst, Cu/ $\beta$ -Mo<sub>2</sub>C-600 was subsequently synthesized (XRD pattern shown in Fig. S3†) and its RWGS performance shown in Fig. S5† was compared with those of other

Table 2 Mo 3d<sub>5/2</sub> binding energies and Mo<sup>2+</sup> contents measured by XPS for  $\beta$ -Mo<sub>2</sub>C-600,  $\beta$ -Mo<sub>2</sub>C-700, and  $\beta$ -Mo<sub>2</sub>C-800 catalysts

Sample	Mo 3d <sub>5/2</sub> (eV)				Mo <sup>2+</sup> content (%)
	Mo <sup>2+</sup> carbide	Mo <sup>δ+</sup> oxycarbide	Mo <sup>4+</sup> oxide	Mo <sup>6+</sup> oxide	
$\beta$ -Mo <sub>2</sub> C-600	—	229.2	229.9	232.7	0
$\beta$ -Mo <sub>2</sub> C-700	228.7	229.1	229.9	232.6	32.0
$\beta$ -Mo <sub>2</sub> C-800	228.6	229.3	—	—	63.2



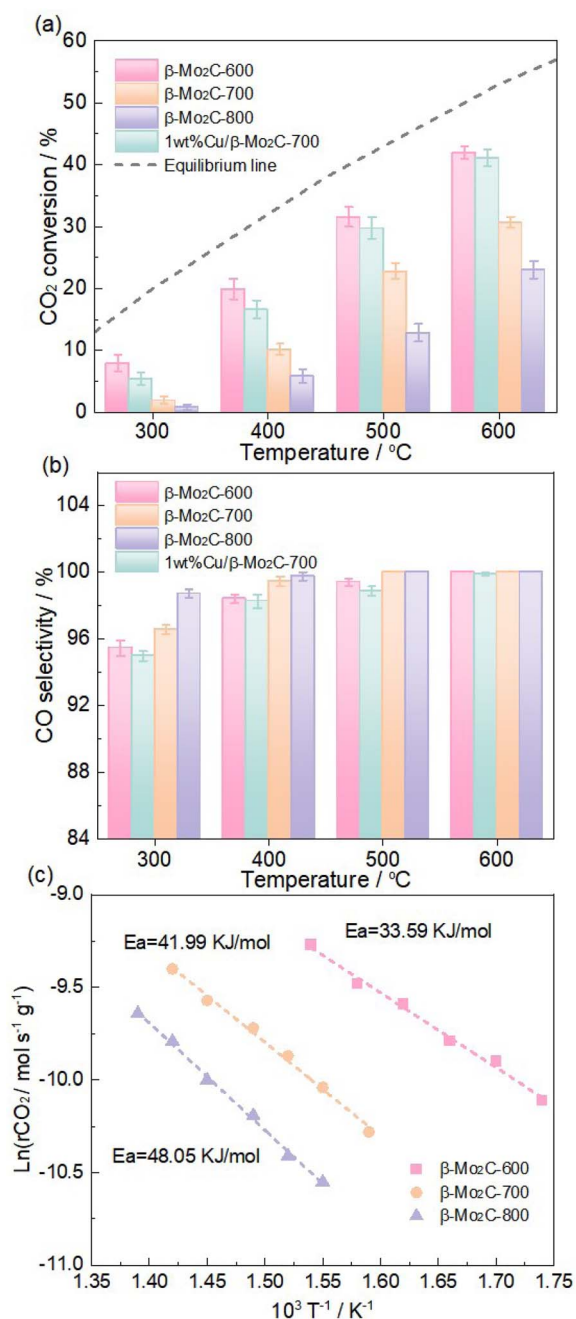


Fig. 5 (a) CO<sub>2</sub> conversion and (b) CO selectivity over β-Mo<sub>2</sub>C-600, β-Mo<sub>2</sub>C-700, and β-Mo<sub>2</sub>C-800 catalysts in the RWGS reaction as well as 1 wt% Cu/β-Mo<sub>2</sub>C-700 catalyst for comparison (reaction conditions: CO<sub>2</sub>/H<sub>2</sub> = 1/2, WHSV = 150 000 cm<sup>3</sup> g<sup>-1</sup> h<sup>-1</sup>, T = 300–600 °C) and (c) Arrhenius plots and E<sub>a</sub> values below 15% of CO<sub>2</sub> conversion.

mainstream catalysts (Table S1† and ref. 41–45). It was clear that the Cu/β-Mo<sub>2</sub>C-600 catalyst exhibited superior activity to traditional Pt and Cu-based as well as Mo<sub>2</sub>C-based catalysts.

The CO adsorption properties of β-Mo<sub>2</sub>C-600, β-Mo<sub>2</sub>C-700, and β-Mo<sub>2</sub>C-800 catalysts were estimated by CO-TPD, as presented in Fig. 6. The CO-TPD profiles revealed an obvious desorption peak at around 870 °C for all samples, consistent with previously reported data.<sup>22</sup> The amount of CO desorption ranked in the order of β-Mo<sub>2</sub>C-600 (69.4 μmol g<sup>-1</sup>) > β-Mo<sub>2</sub>C-700

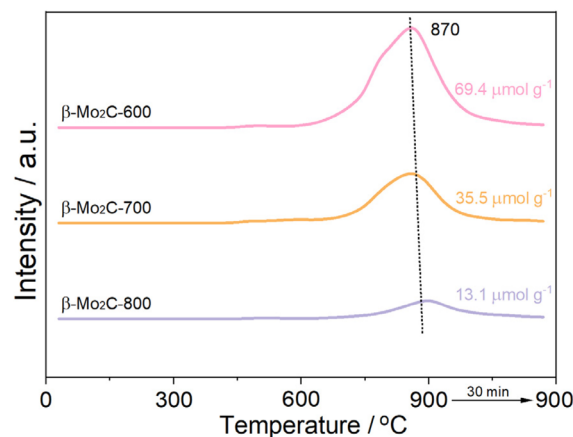


Fig. 6 CO-TPD curves of β-Mo<sub>2</sub>C-600, β-Mo<sub>2</sub>C-700, and β-Mo<sub>2</sub>C-800 catalysts.

(35.5 μmol g<sup>-1</sup>) > β-Mo<sub>2</sub>C-800 (13.1 μmol g<sup>-1</sup>). The observed order showed an opposite trend to their crystallite size variation. The results suggested an inverse relationship between CO affinity and β-Mo<sub>2</sub>C crystallite size, with smaller crystallite size demonstrating stronger CO affinity. In the RWGS reaction, the

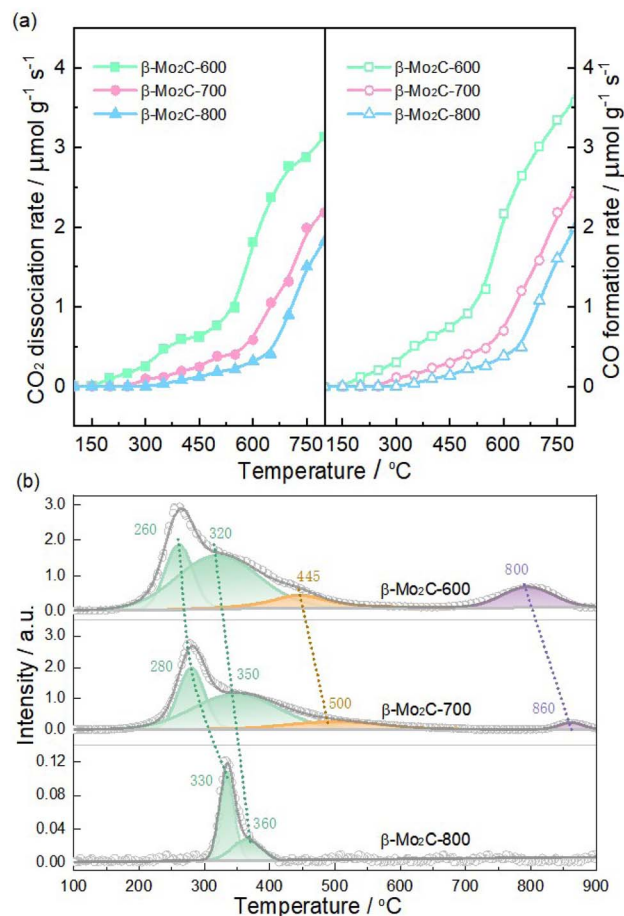


Fig. 7 (a) CO<sub>2</sub>-TPO and (b) H<sub>2</sub>-TPR profiles of passivated β-Mo<sub>2</sub>C-600, β-Mo<sub>2</sub>C-700, and β-Mo<sub>2</sub>C-800 catalysts.



Table 3 The summarized data for the H<sub>2</sub>-TPR in Fig. 7b

Sample	Peak temperature (°C)			Total H <sub>2</sub> consumption (μmol g <sup>-1</sup> )
	Mo <sub>x</sub> OC <sub>y</sub> → Mo <sub>x</sub> C <sub>y</sub>	MoO <sub>3</sub> → MoO <sub>2</sub>	MoO <sub>2</sub> → Mo	
β-Mo <sub>2</sub> C-600	260, 320	445	800	1344.1
β-Mo <sub>2</sub> C-700	280, 350	500	860	934.7
β-Mo <sub>2</sub> C-800	330, 360	—	—	13.1

higher the CO affinity was, the easier the CH<sub>4</sub> formation *via* CO hydrogenation. This was probably the reason why the CO selectivity followed the order: β-Mo<sub>2</sub>C-800 > β-Mo<sub>2</sub>C-700 > β-Mo<sub>2</sub>C-600.

Compared to the associative routes that involved the formation of formate and carboxyl, the redox pathway, Mo<sub>x</sub>C<sub>y</sub> + CO<sub>2</sub> = Mo<sub>x</sub>OC<sub>y</sub> + CO and Mo<sub>x</sub>OC<sub>y</sub> + H<sub>2</sub> = Mo<sub>x</sub>C<sub>y</sub> + H<sub>2</sub>O, had been identified as the key steps for achieving high RWGS activity of Mo carbide.<sup>11,13</sup> Therefore, it became evident that the redox ability of β-Mo<sub>2</sub>C predominantly influenced its RWGS activity. Subsequently, the oxidizability and reducibility of β-Mo<sub>2</sub>C were characterized using CO<sub>2</sub>-TPO and H<sub>2</sub>-TPR techniques, respectively. As depicted in Fig. 7a, all three samples exhibited a consistent increase in CO<sub>2</sub> consumption accompanied by CO generation as the temperature was elevated. It was noteworthy that significant increases in CO<sub>2</sub> dissociation and CO formation rates were observed above 550, 600, and 650 °C for β-Mo<sub>2</sub>C-600, β-Mo<sub>2</sub>C-700, and β-Mo<sub>2</sub>C-800, respectively. These results suggest that severe bulk oxidation occurred in these samples under high-temperature conditions.<sup>33,37</sup> This trend clearly indicated that the catalyst's oxidizability followed the sequence: β-Mo<sub>2</sub>C-600 > β-Mo<sub>2</sub>C-700 > β-Mo<sub>2</sub>C-800, which corresponded with the sequence of their oxophilicity estimated from XPS data. Fig. 7b shows the H<sub>2</sub>-TPR profiles for the passivated β-Mo<sub>2</sub>C-600, β-Mo<sub>2</sub>C-700, and β-Mo<sub>2</sub>C-800 samples and the H<sub>2</sub>-TPR data are summarized in Table 3. The H<sub>2</sub> consumption peaks corresponding to the reduction of these Mo species were evident in the H<sub>2</sub>-TPR profiles. According to XPS results, the β-Mo<sub>2</sub>C-600 and β-Mo<sub>2</sub>C-700 exhibited three oxygen-containing Mo species (Mo<sub>x</sub>OC<sub>y</sub>, MoO<sub>2</sub> and MoO<sub>3</sub>), whereas the β-Mo<sub>2</sub>C-800 showed only one oxygen-containing Mo species (Mo<sub>x</sub>OC<sub>y</sub>). Therefore, the peaks below 360 °C were assigned to the reduction of Mo<sub>x</sub>OC<sub>y</sub>.<sup>7,46</sup> Reduction of MoO<sub>3</sub> to MoO<sub>2</sub> could contribute to H<sub>2</sub> consumption at temperatures above 400 °C,<sup>47</sup> and the reduction of MoO<sub>2</sub> to Mo was expected at temperatures above 800 °C.<sup>48</sup> These reduction peaks associated with Mo<sub>x</sub>OC<sub>y</sub> shifted to higher temperatures in the sequence β-Mo<sub>2</sub>C-600, β-Mo<sub>2</sub>C-700, and β-Mo<sub>2</sub>C-800, indicating a trend of decreasing reducibility: β-Mo<sub>2</sub>C-600 > β-Mo<sub>2</sub>C-700 > β-Mo<sub>2</sub>C-800. Moreover, the total H<sub>2</sub>-consumption values in Table 3 provide additional confirmation of the sequence of oxophilicity determined by XPS. Correlating CO<sub>2</sub>-TPO and H<sub>2</sub>-TPR results with crystallite size analysis suggested that reducing crystallite size can enhance the redox ability of β-Mo<sub>2</sub>C, thereby improving its RWGS activity through the redox pathway.

It was obvious that both Mo<sub>x</sub>C<sub>y</sub> and Mo<sub>x</sub>OC<sub>y</sub> phases served as active sites in the redox pathway, with this unsaturated Mo<sub>x</sub>OC<sub>y</sub>

phase being reported to be more active than Mo<sub>x</sub>C<sub>y</sub>.<sup>15</sup> It was reasonable to deduce that the presence of incompletely carbonized Mo<sub>x</sub>OC<sub>y</sub> in β-Mo<sub>2</sub>C would enhance its RWGS activity. The TEM and H<sub>2</sub>-TPR results (Fig. 2 and 3) revealed that only β-Mo<sub>2</sub>C-600 contained the incompletely carbonized Mo<sub>x</sub>OC<sub>y</sub> species before the reaction, which might contribute to its superior activity compared to β-Mo<sub>2</sub>C-700 and β-Mo<sub>2</sub>C-800. Finally, the β-Mo<sub>2</sub>C-600, β-Mo<sub>2</sub>C-700, and β-Mo<sub>2</sub>C-800 catalysts after the reaction were characterized by XRD and H<sub>2</sub>-TPR (see Fig. S6 and S7†). It can be seen from Fig. S6† that the XRD patterns of used samples resembled those of fresh samples, indicating these β-Mo<sub>2</sub>C catalysts can keep their bulk structure well at 600 °C in RWGS. Note that the H<sub>2</sub>-TPR results indicated H<sub>2</sub> consumption below 400 °C for all three used samples. The H<sub>2</sub> consumption values followed the order of β-Mo<sub>2</sub>C-600 > β-Mo<sub>2</sub>C-700 > β-Mo<sub>2</sub>C-800, suggesting that the amount of Mo<sub>x</sub>OC<sub>y</sub> decreased in the same sequence. This finding further confirmed the correlation between the Mo<sub>x</sub>OC<sub>y</sub> content in β-Mo<sub>2</sub>C and its RWGS activity. Therefore, in addition to crystallite size, the Mo<sub>x</sub>OC<sub>y</sub> content was proposed to be another key factor influencing the RWGS activity of β-Mo<sub>2</sub>C catalyst.

## 4 Conclusions

A clear correlation was observed between the carbonization synthesis temperature and the RWGS activity, with the activity following the order: β-Mo<sub>2</sub>C-600 > β-Mo<sub>2</sub>C-700 > β-Mo<sub>2</sub>C-800. Even β-Mo<sub>2</sub>C-600 showed slightly superior RWGS activity compared to Cu-doped β-Mo<sub>2</sub>C-700 under similar reaction conditions. It was proposed that crystallite size and Mo<sub>x</sub>OC<sub>y</sub> content were key factors influencing the RWGS activity of β-Mo<sub>2</sub>C. These factors can effectively regulate the redox properties of β-Mo<sub>2</sub>C catalyst, thereby affecting its catalytic activity in the RWGS reaction. This study underscored a strategy to enhance the RWGS activity of β-Mo<sub>2</sub>C catalysts by reducing crystallite size or increasing the Mo<sub>x</sub>OC<sub>y</sub> content.

## Data availability

The data supporting this article have been included as part of the ESI.†

## Conflicts of interest

There are no conflicts to declare.



## Acknowledgements

The work was supported by the National Natural Science Foundation of China (No. 21978125), the Project of Guangdong Province Department of Education (No. 2023ZDZX3035) and the Project of Liaoning Province Department of Education (No. LJ212410148022).

## Notes and references

- 1 D. Zagoraios, N. Kokkinou, G. Kyriakou and A. Katsaounis, *Catal. Sci. Technol.*, 2022, **12**, 1869–1879.
- 2 A. R. Querido, L. P. L. Gonçalves, Y. V. Kolen'ko, M. F. R. Pereira and O. S. G. P. Soares, *Catal. Sci. Technol.*, 2023, **13**, 3606–3613.
- 3 C. F. Holder, J. R. Morse, P. M. Barboun, A. R. Shabaev, J. W. Baldwin and H. D. Willauer, *Catal. Sci. Technol.*, 2023, **13**, 2685–2695.
- 4 S. Posada-Pérez, F. Viñes, P. J. Ramirez, A. B. Vidal, J. A. Rodriguez and F. Illas, *Phys. Chem. Chem. Phys.*, 2014, **16**, 14912–14921.
- 5 M. D. Porosoff, X. Yang, J. A. Boscoboinik and J. G. Chen, *Angew. Chem., Int. Ed.*, 2014, **53**, 6705–6709.
- 6 L. Wang, H. Wang, H. Huang, T. Yun, C. Song and C. Shi, *Adv. Funct. Mater.*, 2024, **34**, 2309850.
- 7 X. Liu, C. Kunkel, P. R. Piscina, N. Homs, F. Viñes and F. Illas, *ACS Catal.*, 2017, **7**, 4323–4335.
- 8 J. Gao, Y. Wu, C. Jia, Z. Zhong, F. Gao, Y. Yang and B. Liu, *Catal. Commun.*, 2016, **84**, 147–150.
- 9 M. D. Porosoff, S. Kattel, W. Li, P. Liu and J. Chen, *Chem. Commun.*, 2015, **51**, 6988–6991.
- 10 M. Attwood, H. Akutsu, L. Martin, D. Cruickshank and S. S. Turner, *Dalton Trans.*, 2019, **48**, 90–98.
- 11 M. A. Khoshooei, X. Wang, G. Vitale, F. Formalik, K. O. Kirlikovali, R. Q. Snurr, P. Pereira-Almao and O. K. Farha, *Science*, 2024, **384**, 540–546.
- 12 M. Dixit, X. Peng, M. D. Porosoff, H. D. Willauer and G. Mpourmpakis, *Catal. Sci. Technol.*, 2017, **7**, 5521–5529.
- 13 A. Jurado, Á. Morales-García, F. Viñes and F. Illas, *ACS Catal.*, 2022, **12**, 15658–15667.
- 14 X. Du, R. Li, H. Xin, Y. Fan, C. Liu, X. Feng, J. Wang, C. Dong, C. Wang, D. Li, Q. Fu and X. Bao, *Angew. Chem., Int. Ed.*, 2024, e202411761.
- 15 X. Sun, J. Yu, H. Zada, Y. Han, L. Zhang, H. Chen, W. Yin and J. Sun, *Nat. Chem.*, 2024, **16**, 2044–2053.
- 16 F. G. Baddour, E. J. Roberts, A. T. To, L. Wang, S. E. Habas, D. A. Ruddy, N. M. Bedford, J. Wright, C. P. Nash, J. A. Schaidle, R. L. Brutchey and N. Malmstad, *J. Am. Chem. Soc.*, 2020, **142**, 1010–1019.
- 17 X. Zhang, Y. Liu, M. Zhang, T. Yu, B. Chen, Y. Xu, M. Crocker, X. Zhu, Y. Zhu, R. Wang, D. Xiao, M. Bi, D. Ma and C. Shi, *Chem*, 2020, **6**, 3312–3328.
- 18 J. Lu, S. Zhang, H. Zhou, C. Huang, L. Xia, X. Liu, H. Luo and H. Wang, *Acta Phys. Chim. Sin.*, 2023, **39**, 2302021.
- 19 M. D. Porosoff, J. W. Baldwin, X. Peng, G. Mpourmpakis and H. D. Willauer, *ChemSusChem*, 2017, **10**, 2408–2415.
- 20 Y. Ma, Z. Guo, Q. Jiang, K. H. Wu, H. Gong and Y. Liu, *J. Energy Chem.*, 2020, **50**, 37–43.
- 21 W. Marquart, S. Raseale, G. Prieto, A. Zimina, B. B. Sarma, J. D. Grunwaldt, M. Claeys and N. Fischer, *ACS Catal.*, 2021, **11**, 1624–1639.
- 22 Q. Rong, W. Ding, G. Liu, Z. Zhang and Z. Yao, *Catal. Sci. Technol.*, 2023, **13**, 6360–6365.
- 23 A. G. Galallah, M. K. Albolqany, A. E. Rashed, W. Sadik, A. G. El-Demerdash and A. A. El-Moneim, *J. Environ. Chem. Eng.*, 2024, **12**, 113380.
- 24 S. Cao, Z. Guan, Y. Ma, B. Xu, J. Ma, W. Chu, R. Zhang, G. Giambastiani and Y. Liu, *ACS Catal.*, 2024, **14**, 10939–10950.
- 25 X. Zhang, X. Zhu, L. Lin, S. Yao, M. Zhang, X. Liu, X. Wang, Y. W. Li, C. Shi and D. Ma, *ACS Catal.*, 2017, **7**, 912–918.
- 26 E. Heracleous, V. Koidi and A. A. Lappas, *Catal. Sci. Technol.*, 2021, **11**, 1467–1480.
- 27 Q. Zhang, L. Pastor-Pérez, W. Jin, S. Gu and T. R. Reina, *Appl. Catal., B*, 2019, **244**, 889–898.
- 28 J. Xu, X. Gong, R. Hu, Z. Liu and Z. Liu, *Mol. Catal.*, 2021, **516**, 111954.
- 29 M. Figueras, R. A. Gutiérrez, F. Viñes, P. J. Ramirez, J. A. Rodriguez and F. Illas, *ACS Catal.*, 2021, **11**, 9679–9687.
- 30 W. Zhang, A. Vidal-López and A. Comas-Vives, *Front. Chem.*, 2023, **11**, 11444189.
- 31 R. Liu, C. Chen, W. Chu and W. Sun, *Materials*, 2022, **15**, 3775.
- 32 A. Hanif, T. Xiao, A. P. E. York, J. Sloan and M. L. H. Green, *Chem. Mater.*, 2002, **14**, 1009–1015.
- 33 P. Liang, H. Gao, Z. Yao, R. Jia, Y. Shi, Y. Sun, Q. Fan and H. Wang, *Catal. Sci. Technol.*, 2017, **7**, 3312–3324.
- 34 Z. Yao, J. Jiang, Y. Zhao, F. Luan, J. Zhu, Y. Shi, H. Gao and H. Wang, *RSC Adv.*, 2016, **6**, 19944–19951.
- 35 H. Gao, Z. Yao, Y. Shi and S. Wang, *Catal. Sci. Technol.*, 2018, **8**, 697–701.
- 36 H. Wang, S. Liu, B. Liu, V. Montes, J. M. Hill and K. J. Smith, *J. Solid State Chem.*, 2018, **258**, 818–824.
- 37 H. Gao, Z. Yao, Y. Shi, R. Jia, F. Liang, Y. Sun, W. Ma and H. Wang, *Inorg. Chem. Front.*, 2018, **5**, 90–99.
- 38 A. Kurlov, E. B. Deeva, P. M. Abdala, D. Lebedev, A. Tsoukalou, A. Comas-Vives, A. Fedorov and C. R. Müller, *Nat. Commun.*, 2020, **11**, 1–11.
- 39 S. Upadhyay and O. P. Pandey, *Int. J. Hydrogen Energy*, 2020, **45**, 27114–27128.
- 40 L. Yang, L. Pastor-Pérez, J. J. Villora-Pico, A. Sepúlveda-Escribano, F. Tian, M. Zhu, Y. F. Han and T. R. Reina, *ACS Sustainable Chem. Eng.*, 2021, **9**, 12155–12166.
- 41 S. Kim, H. Lee and S. Hong, *Appl. Catal., A*, 2012, **423–424**, 100–107.
- 42 C. S. Chen, W. H. Cheng and S. S. Lin, *Catal. Lett.*, 2000, **68**, 45–48.
- 43 L. Wang, S. Zhang and Y. Liu, *J. Rare Earths*, 2008, **26**, 66–70.



- 44 X. Pan, H. Sun, M. Ma, H. Liao, G. Zhan, K. Wang, M. Fan, J. Xu, L. Ding, K. Sun and J. Jiang, *Biochar*, 2024, **6**, 93.
- 45 M. Zhang, Y. Zhu, J. Yan, J. Xie, T. Yu, M. Peng, J. Zhao, Y. Xu, A. Li, C. Jia, L. He, M. Wang, W. Zhou, R. Wang, H. Jiang, C. Shi, J. Rodriguez and D. Ma, *Angew. Chem., Int. Ed.*, 2025, **64**, e202418645.
- 46 G. Wang, J. A. Schaidle, M. B. Katz, Y. Li, X. Pan and L. T. Thompson, *J. Catal.*, 2013, **304**, 92–99.
- 47 P. Sun, F. Teng, Z. Yang, X. Yang, S. Zhai, S. Liang, W. Gu, W. Hao and S. Shi, *J. Mater. Chem. C*, 2020, **8**, 2475–2482.
- 48 P. Chen, Z. Xie, Z. Zhao, J. Li, B. Liu, B. Liu, X. Fan, L. Kong and X. Xiao, *Catal. Sci. Technol.*, 2021, **11**, 4083–4097.

